






On the relationship between the plasma characteristics, the microstructure and the optical properties of reactively sputtered TiO₂ thin films

M Michiels^{1,2} , A Hemberg¹, T Godfroid^{1,3} , O Douheret¹, J L Colaux⁴, P Moskovkin⁴, S Lucas⁴ , A Caillard⁵, A-L Thomann⁵, P Laha⁶, H Terryn⁶, M Voué^{7,*}, A Panepinto², R Snyders^{1,2}  and S Konstantinidis² 

¹ Materia Nova Research Center, 3 Avenue Nicolas Copernic, Parc Initialis, 7000 Mons, Belgium

² Chimie des Interactions Plasma-Surface (ChIPS), CIRMAP, Université de Mons, 23 Place du Parc, 7000 Mons, Belgium

³ Materia Nova Research Center, 137 Fritz-Müller-Straße, 73730 Esslingen, Germany

⁴ Namur Institute of Structured Matter (NISM), Synthesis, Irradiation and Analysis of Materials Platform (SIAM), University of Namur, 61 Rue de Bruxelles, 5000 Namur, Belgium

⁵ Groupe de Recherches sur l'Energétique des Milieux Ionisés (GREMI), Université d'Orléans, CNRS, 45067 Orléans cedex 2, France

⁶ Electrochemical and Surface Engineering (SURF), Vrije Universiteit Brussel, 2 Pleinlaan, 1050 Brussel, Belgium

⁷ Materials Physics and Optics, University of Mons, 20 Place du Parc, Mons 7000, Belgium

E-mail: Michel.VOUE@umons.ac.be

Received 17 March 2021, revised 18 June 2021

Accepted for publication 6 July 2021

Published 29 July 2021



Abstract

A titanium target was reactively sputtered in an Ar/O₂ atmosphere by (i) conventional direct current magnetron sputtering (DCMS), (ii) high-power impulse magnetron sputtering (HiPIMS), and (iii) bipolar HiPIMS (BPH) discharges for the deposition of titanium dioxide thin films without intentional heating and biasing. In the HiPIMS and BPH cases, the peak current density was set to either 0.32 A cm⁻² or 0.86 A cm⁻². The time-averaged power density delivered to the plasma was set to ≈1.2 W cm⁻² in each case. For the BPH discharge, a positive pulse of +300 V was applied after the negative pulse to accelerate the positive ions toward the substrate. Energy-resolved mass spectrometry analysis has shown a low-energy peak for DCMS while a high energy tail extending in the range of several tens of eV was observed with HiPIMS. In the BPH discharge, the energy reached ≈300 eV for Ti⁺ ions, which is in agreement with the applied positive potential. According to the x-ray diffraction patterns, amorphous coatings were obtained with DCMS, while rutile TiO₂ was obtained with both HiPIMS and BPH. However, in the BPH case, diffractograms were characterized by more intense high-angle diffraction peaks highlighting a modification of the growth process for these conditions. Rutherford backscattering spectrometry analysis has shown that a higher amount of argon atoms were incorporated into the TiO₂ films which are found to be slightly understoichiometric for the BPH discharge. It was also found that the refractive index, *n*, varied as a function of the sputtering regime with the highest value obtained in the HiPIMS case (*n* = 2.73 at 550 nm). Finally, the experimentally determined optical data were compared to the ones extracted from NASCAM simulations which are found in good agreement except for the BPH case.

* Author to whom any correspondence should be addressed.

Supplementary material for this article is available [online](#)

Keywords: titanium dioxide, reactive magnetron sputtering, bipolar HiPIMS, BPH, modeling, ellipsometry, plasma diagnostics

(Some figures may appear in colour only in the online journal)

1. Introduction

Titanium dioxide (TiO_2) has a wide range of applications in optics, catalysis or electronics [1–3]. In bulk form, TiO_2 is a polymorphous material existing in three crystalline structures: anatase, rutile and brookite. Tetragonal structures are formed for both anatase and rutile phases, while brookite is orthorhombic [4]. However, in the form of thin films, only anatase and rutile structures are usually observed [5].

Anatase TiO_2 coatings are synthesized for their interesting properties such as high corrosion resistance and chemical stability, wide band gap as well as excellent optical transparency in the visible and near infrared regions [6–8]. The rutile phase, which is often synthesized at high temperature, typically above 600°C [4], is mainly used in optical applications for its high refractive index (2.75 at 550 nm [9]). As the refractive index varies with wavelength, it might also be influenced by many other parameters such as the morphology of the film surface (correlated to the thickness), film density or temperature [6, 10, 11].

More particularly in the case of photocatalytic applications, the control of the TiO_2 crystalline constitution is a key parameter for improving the efficiency of the photocatalytic reaction which is generally limited by the high recombination rate of photoinduced electron–hole pairs [3, 12]. In this regard, a film composed of $\approx 60\%$ anatase and $\approx 40\%$ rutile exhibits optimal performances (50% improved photo-reactivity) as compared to pure anatase as shown by Su *et al* [13].

The deposition of TiO_2 films by means of physical vapor deposition (PVD) techniques has been demonstrated in numerous studies [9, 14–17] showing that the process parameters such as pressure, gas mixture, magnetic field configuration, power delivered to the plasma, etc influence the film growth and consequently the film properties. Numerous authors [18–22] have shown that replacing the direct current (DC) plasma source by a high-power impulse magnetron sputtering (HiPIMS) one, allowing to deliver at the cathode short electrical pulses with very high power density, dramatically changes the film density and phase constitution since the ionization degree and kinetic energy of the film-forming species are significantly increased [20]. For HiPIMS discharges, pure rutile films are generally characterized by larger grains and smoother films [23] than those for direct current magnetron sputtering (DCMS) films, while (pulsed) DC magnetron sputtering using similar working conditions mainly leads to the growth of amorphous or anatase films [3, 9, 17]. Furthermore, in the HiPIMS case, the rutile films can be synthesized without (post-)annealing treatment [9]. The energy transfer during the film growth phase is therefore a key parameter for controlling

the structural and optical properties of TiO_2 films [16]. Many contributions can participate to the energy transfer during the deposition by magnetron-based processes: (primary and secondary) electrons, heavy particles bombardment (i.e. fast neutrals and ions) as well as electromagnetic radiations originating from the plasma bulk and from the heated target surface [16, 24, 25].

More recently, bipolar HiPIMS (BPH) started attracting attention since this technique aims to control the ions kinetic energy without applying a substrate bias. In the BPH case, the negative (plasma) pulse, necessary for sputtering and ionizing the metal atoms, is followed by a positive voltage pulse to accelerate the positive ions towards the substrate surface [26]. Plasma diagnostics of BPH discharges [26–32] as well as the analysis of film properties [33] have been reported in the literature.

In this study, we chose the reactive sputtering of TiO_2 as a model system. High positive voltage was applied at the cathode (+300 V) during BPH as compared to other works [31–33]. First, energy-resolved mass spectrometry was carried out for DC, HiPIMS and BPH plasmas in order to establish the relationship between the plasma phase and film growth for a broad range of plasma parameters. Secondly, the deposition of ≈ 100 nm thick TiO_2 films was carried out for each case to study how the plasma conditions influence the film properties (i.e. composition, microstructural and optical properties). Energy resolved mass spectrometry data were also used as an input for kinetic Monte-Carlo—based modeling of the film growth from which the film refractive index was extracted and compared to ellipsometry results.

2. Experimental setup

2.1. Vacuum chambers

In our study, two different vacuum chambers equipped with a balanced magnetron source were utilized with the aim to compare and validate the mass spectrometry results. The first vacuum chamber (VC1) is a cylindrical stainless-steel high vacuum chamber, 250 mm in diameter and 450 mm height, as schematized in figure 1. A dry primary pump producing a vacuum level of $\approx 10^{-2}$ Torr was connected to a turbomolecular pump (Edwards nXDS6i 260 W) to reach a residual pressure of $\approx 10^{-7}$ Torr. The total working pressure was maintained at 5 mTorr (0.67 Pa) by a closed-loop throttle valve for all experiments. The Ar (99.999% purity) and O_2 (99.999% purity) gas mixture was introduced into the chamber at total constant flow rate of 44 sccm by means of a mass flow controller (Brooks Instrument 0154) with a constant ratio O_2/Ar set to 8%. This ratio ensured the poisoned regime to be reached

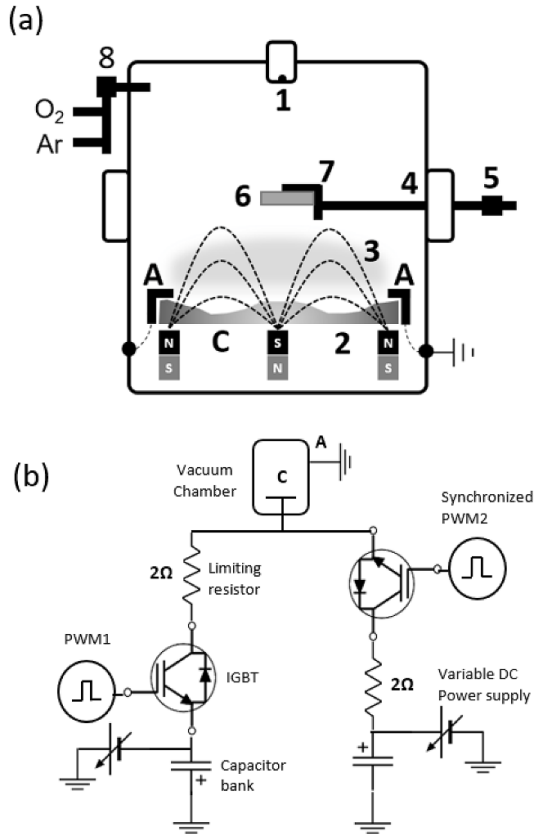


Figure 1. Schematic views of (a) the PVD process chamber (VC1, not to scale) and (b) the lab-made half bridge power supply for the generation of BPH pulses. Pulse width modulation (PWM) is generated by microcontroller to produce isolated synchronized signals for driving the insulated gate bipolar transistors (IGBTs). In HiPIMS mode, only the left arm of the half bridge is utilized. The numbers correspond to (1) the 100 μm in diam. mass spectrometer orifice, (2) the Ti target, (3) the lines of forces of magnetic field, (4) the load-lock chamber for sample introduction, (5) the connection to the substrate holder, (6) the Si substrate, (7) the substrate holder and (8) the gas inlets. The notations (A) and (C) are used for anode and cathode, respectively.

whatever the DC, HiPIMS or BPH regime (the transition to this poisoned regime occurred below 5% in each sputtering regime in our conditions). A balanced magnetron source, supporting a 4-inch circular planar Ti target (99.99% purity), was placed at the bottom of the vacuum chamber with the substrate located in front of the target, 80 mm above. The substrate holder was electrically grounded in all experiments for the sake of comparison. The ≈ 100 nm thick films were deposited onto low resistivity single crystal silicon wafers ($5 \times 10^{-3} \Omega \cdot \text{cm}$, $\langle 100 \rangle$ orientation). Dust from the substrate surface was removed using a spray of dry air.

The second vacuum chamber (VC2), a six-way cross-shaped stainless-steel (400 mm long with ISO200-K flanges) chamber, was mainly dedicated to complementary mass spectrometry measurements. A residual pressure of 5×10^{-7} Torr using a turbo-molecular pump (500 l/s Pfeiffer Vacuum) was reached. After gas introduction using Bronkhorst mass flow meters, the working pressure was fixed to 5 mTorr using a high vacuum gate valve. The flow rates were tuned to 40

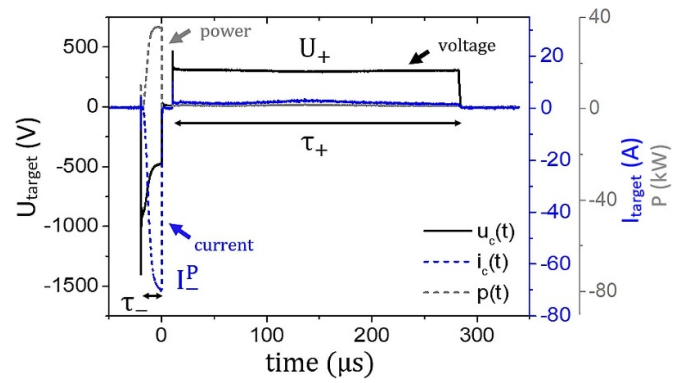


Figure 2. General voltage (black curve) and current (blue curve) waveforms during the BPH discharge. A voltage drop exists during the negative pulse which is induced by series resistors as shown in figure 1(b). The peak power value at the end of the negative pulse is ≈ 33 kW (grey curve).

and 3.5 sccm, for Ar and O₂ respectively, ensuring a constant ratio O₂/Ar of 8%. The circular balanced magnetron (2 inches ONYX from Angström science) was equipped with a 3 mm thick Ti target.

The films were deposited in VC1 using two peak currents, i.e. 26 and 70 A. In order to obtain energy-resolved mass spectrometry measurements in VC2 matching with the plasma deposition conditions implemented in VC1, the plasma analysis measurements were carried out in VC2 by applying a peak current density identical to the one applied in VC1, namely $J_{P1} = 0.32 \text{ A cm}^{-2}$ (corresponding to $I_{P1}^c = 26 \text{ A}$ in VC1) and $J_{P2} = 0.86 \text{ A cm}^{-2}$ (corresponding to $I_{P2}^c = 70 \text{ A}$ in VC1). In the DCMS case, an Advanced Energy MDK 1.5 K power supply was utilized in VC1 while a Kurt J. Lesker PD500X3 was utilized in VC2. In both HiPIMS and BPH cases, a lab-made power supply more precisely described in the next section was utilized.

2.2. HiPIMS and BPH plasma source

The electronic circuitry shown in figure 1(b) was based on a half bridge topology allowing short bipolar high-power pulses to be generated at the cathode (labeled C on the figure). The time-evolution of the cathode voltage, cathode current and power supplied to the plasma in our conditions are shown in figure 2. It is important to note that 2Ω resistors were utilized for limiting the peak current flowing through IGBTs resulting in an ohmic voltage drop as observed during the negative pulse (black curve in figure 2). In our study, the negative pulse duration was fixed at 20 μs and the pulse repetition frequency and discharge voltage were modified independently (see table 1). In VC1, the DC average power was fixed at 100 W corresponding to the power density on the target surface of $\approx 1.2 \text{ W} \cdot \text{cm}^{-2}$. In the HiPIMS and BPH cases, the time-averaged power, P_{av} , (varying from 100 to 150 W) was calculated with a 40 ns time resolution using equation (1).

$$P_{av} = \frac{1}{T} \int_0^T u_c(t) \cdot i_c(t) dt \quad (1)$$

Table 1. Main electrical parameters used in this work for film deposition in VC1 and for discharges operated in the poisoned regime (0.66 Pa and 8% of O₂).

	U ₋ (V)	U ₊ (V)	I ₋ ^p (A)	J _P (A·cm ⁻²)	f (Hz)	P _{av} (W)
DCMS	—	—	—	3.5 × 10 ⁻³	—	100
HIP26A	670	0	26	3.2 × 10 ⁻¹	505	106
HIP70A	870	0	72	8.6 × 10 ⁻¹	143	115
BPH26A	670	300	26	3.2 × 10 ⁻¹	505	145
BPH70A	870	300	70	8.6 × 10 ⁻¹	143	150

where T is the pulse repetition period in HiPIMS or BPH regime, $u_c(t)$ and $i_c(t)$ are the instantaneous cathode voltage and current, respectively (see figure 2).

It has to be mentioned that, for the BPH discharges in VC1, the power fraction delivered to the plasma during the positive pulse was $\approx 40\%$ resulting in the increase of the average power in this case (i.e. 150 W) while the power fraction was $\approx 27\%$ in VC2. Note that P_{av} was varied by $\pm 5\%$ during the deposition time.

A wide bandwidth 1 MHz Tektronix TCP303 Hall effect current probe combined with a TCPA300 amplifier was connected to a Tektronix DPO4034 digital oscilloscope to measure the discharge current while the discharge voltage was measured with a Tektronix high voltage probe P5100. It is important to note that the discharge voltage was measured directly at the cathode and short oscillations at the beginning of both negative and positive voltage pulses were observed. These oscillations, however, did not affect the results described in this work.

In the HiPIMS and BPH cases, the samples were called HIP26A, BPH26A, HIP70A, and BPH70A, with the numbers corresponding to peak current values during the negative pulse, $I_-^p = 26$ A and $I_-^p = 70$ A, respectively. For clarity, this notation was utilized in the rest of the paper while further information about the definition of BPH parameters can be found elsewhere [30]. In the BPH case, the delay between the negative and the positive pulses, τ_{\pm} , was fixed at 10 μ s and the positive pulse width, τ_+ , was fixed at 250 μ s. For HIP26A and BPH26A, the value of the negative voltage, U₋, was set to 670 V while for HIP70A and BPH70A, U₋ = 870 V, as summarized in table 1.

2.3. Plasma diagnostics

In VC1, the relative ion density in the magnetron discharge was measured by a differentially pumped HIDEN Analytical HAL 7 EQP100 energy-resolved mass spectrometer enabling ion energy scans from 0 to 100 eV in 0.05 eV/charge steps. The electrically grounded extraction orifice, 100 μ m in diameter, was located at 160 mm above the magnetron cathode on its axis of symmetry, i.e. 80 mm away from the position of substrate holder.

In VC2, the energy resolved mass spectrometer (Hiden Analytical, EQP1000) enabling ion energy scans from 0 to 1000 eV faced the magnetron center at a distance of 90 mm whereas a 200 μ m grounded orifice was used. An auto-tune procedure was performed for each species [34, 35] in different

eV/charge steps (i.e. 0.1, 0.2 and 0.4 for DCMS, HiPIMS, and BPH cases respectively) in order to adjust the different internal parameters of the mass spectrometer and to optimize the signal intensity.

2.4. Film characterization

The film morphology was observed using a field emission gun scanning electron microscope (FEG-SEM Hitachi SU8020). The electron accelerating voltage was kept constant at 3 kV and a secondary electron detector allowed the sample morphology to be observed.

The surface roughness was measured by Tapping Mode atomic force microscopy (AFM) with a Mutlimode 8 from Bruker, equipped with a Nanoscope V controller and using etched Si probes from Nanosensors (reference PPP-NCHR).

The film thickness was determined by contact profilometer (Veeco 150 Dektak apparatus) from which the deposition rate was calculated as summarized in table 2.

The phase constitution of the samples was analyzed by grazing incidence x-ray diffraction (GIXRD) using a PANalytical Empyrean diffractometer working with Cu K _{α} 1 radiation ($\lambda = 0.1546$ nm) in grazing configuration with an incidence angle of 0.5°. The x-ray source voltage was fixed at 45 kV and the current at 40 mA. Diffraction data post-treatment was carried out using commercial Panalytical Highscore software for phase identification as well as for crystal average size (D) calculation based on the Scherrer equation:

$$D = \frac{\lambda \cdot K}{\beta \cdot \cos(\theta)} \quad (2)$$

where λ is the wavelength of CuK _{α} radiation, K is the particle shape factor, β is the full width at half maximum of the intensity peak and θ is the Bragg angle.

The elemental composition was obtained by Rutherford backscattering spectrometry (RBS). Each sample was analyzed using an alpha beam at 3.05 MeV for sensitivity to oxygen content. The spectra were collected by two passivated implanted planar silicon detectors at 135° and 165° and recorded using MPA3. The detectors were calibrated using three incident energies ranging from 2 to 3.05 MeV using a SnO₂ standard glass. The electronic calibration as well as the ratio between the solid angles of these detectors were determined by fitting those calibration spectra with DataFurnace [36]. All the spectra were acquired on the same location on the sample and were fitted self-consistently with DataFurnace, using the stopping power provided by SRIM database (www.srim.org)

Table 2. Metal-ion to gas-ion ratios and effective ion mean energies calculated on the actual discharge parameters. The deposition rates R_D calculated using profilometer data (expressed in $\text{nm}\cdot\text{min}^{-1}$) and R_D calculated using RBS data (expressed in $\text{at}\cdot\text{cm}^{-2}\cdot\text{s}^{-1}$) in DCMS, HiPIMS and BPH regimes are shown.

	$\frac{\text{Ti}^+}{\text{Ar}^+}$ (%)	$\frac{\text{Ti}^+}{\text{Ar}^+ + \text{O}^+}$ (%)	$\langle \epsilon_{\text{Ar}^+} \rangle$ (eV)	$\langle \epsilon_{\text{Ti}^+} \rangle$ (eV)	$\langle \epsilon_{\text{O}^+} \rangle$ (eV)	$\langle \epsilon_{\text{Ar}^{2+}} \rangle$ (eV)	$\langle \epsilon_{\text{Ti}^{2+}} \rangle$ (eV)	$\langle \epsilon_{\text{O}^{2+}} \rangle$ (eV)	R_D ($\text{nm}\cdot\text{min}^{-1}$)	R_D ($10^{14}\text{at}\cdot\text{cm}^{-2}\cdot\text{s}^{-1}$)
DCMS	0.2	0.2	1.4	6.4	5.4	4.1	11	10.9	0.78	1.67
HIP26A	26	5.8	3.3	7.2	7.6	10.9	12.3	15.7	0.55	1.22
HIP70A	—	—	—	—	—	—	—	—	0.21	0.56
BPH26A	0.4	0.3	226.2	203.3	132.5	528.3	460.0	53.9	0.49	1.22
BPH70A	7.5	2.7	279.1	184.2	164.6	582.6	500.0	67.3	0.19	0.52

as well as the *evaluated* cross-section functions available on the SigmaCalc [37] website (<http://sigmacalc.iate.obnisk.ru/>). Additionally, the film density was derived from the RBS data combined with the film thickness (see section 3.3).

The complex refractive indices of the samples were determined from spectroscopic ellipsometry measurements performed at two incidence angles (70° and 75°) with a rotating compensator spectroscopic ellipsometer (from J A Woollam Co. Inc. M2000x), measuring in the visible wavelength range (450–750 nm). The analysis software used was CompleteEASE 5.04, also from J A Woollam Co., Inc. The data analysis was done by creating a basic 3-layers model (Si: crystalline silicon substrate; SiO_2 : native silicon oxide layer; TiO_2) using CompleteEase database values for the Si substrate, SiO_2 , and pure TiO_2 (Cody-Lorentz oscillators) and then allowing the software to simulate the best fit parameters for each layer.

Kinetic Monte Carlo simulations were performed with the NASCAM software package as described in detail by Tonneau *et al* [38]. The relative number of atoms and ions coming to the substrate, as extracted from mass spectrometry measurements for different deposition conditions, served as input data for those simulations finally allowing the computation of the microstructure and refractive index of the TiO_2 coatings.

3. Results and discussions

3.1. Energy-resolved mass spectrometry

In the present work, two different vacuum chambers were used at the same pressure and average power (the power density was $\approx 1.2 \text{ W}\cdot\text{cm}^{-2}$) because, as explained in the materials and method section, the VC2 was equipped with a mass spectrometer that enabled detecting ions with kinetic energies up to 1000 eV. In VC1, the energy-resolved mass spectrometer was limited to 100 eV which is not sufficient when, during a BPH process, U_+ is set above +100 V and/or if multiple charged ions must be detected. The Ar^+ , Ti^+ and O^+ ion energy distribution functions (IEDFs) obtained in both vacuum chambers are given in figure 3.

Despite the absolute values of the mean energies, energy maxima and ion counts (extracted from the IEDFs) were not identical (see supplementary materials, available online at stacks.iop.org/JPD/54/415202/mmedia), the evolution of the IEDF of Ar^+ , O^+ and Ti^+ ions was qualitatively very

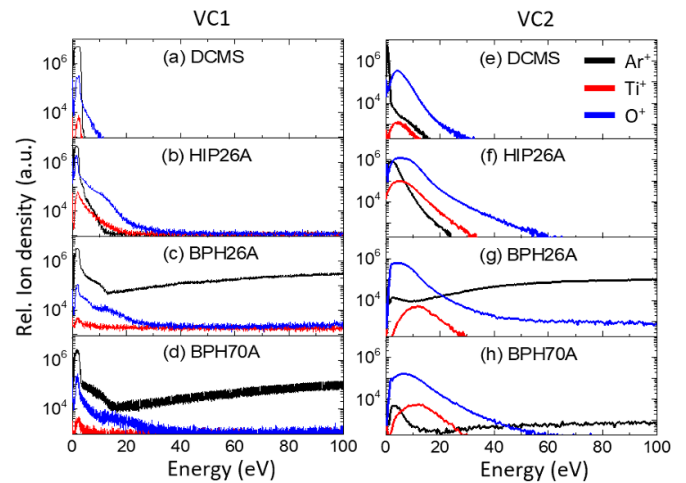


Figure 3. Time-averaged MS measurements of Ar^+ , Ti^+ and O^+ between 0 and 100 eV in first (VC1, left column) and second (VC2, right column) vacuum chamber in the DCMS (a), (e), HiPIMS (b), (f) and BPH (c) and (d), (g), (h) discharges. The change in IEDF shape can be related to the distance between target and mass spectrometer head (160 mm for VC1 and 90 mm for VC2).

similar when going from the DCMS regime to the BPH regime whatever the data were acquired in VC1 or VC2 (in the 0–100 eV range). Indeed, in DCMS and HiPIMS regimes, typical features of the IEDFs can be found in figures 3(a), (e) and 3(b), (f), respectively. In the BPH case (see figures 3(c), (g) and 3(d), (h)), however, an important part of the metal ion population was accelerated to higher energy corresponding to U_+ . This explains why the decrease of the Ti^+ signal intensity (see red curves) is observed with BPH in the 0–100 eV range as compared to the HiPIMS case [28]. This mass spectrometry study demonstrates that the IEDFs acquired in the VC2 can be used for discussing the evolution of the properties of the films deposited in VC1 in DCMS, HiPIMS and BPH regimes.

The time-averaged Ar^+ , Ar^{2+} , Ti^+ , Ti^{2+} , O^+ and O^{2+} IEDFs measured in VC2 are given in figure 4 for the studied discharges. From these measurements, the ion population as well as the population ratios of Ti^+/Ar^+ and $\text{Ti}^+/(Ar^+ + O^+)$ were calculated by integrating the measured IEDFs while the average ion energy $\langle \epsilon \rangle$ was determined using the equation (3) below:

$$\langle \epsilon \rangle = \frac{\int_0^\infty \epsilon F(\epsilon) d\epsilon}{\int_0^\infty F(\epsilon) d\epsilon} \quad (3)$$

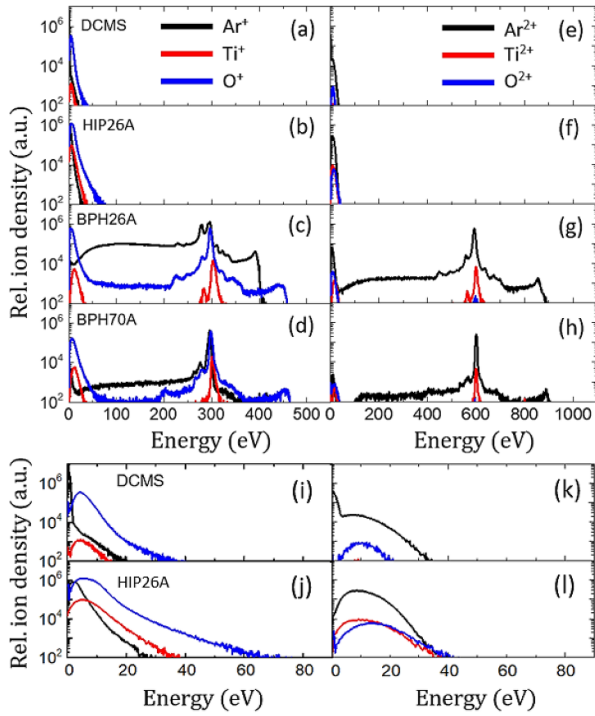


Figure 4. Results of the time-averaged MS measurements in VC2 for Ar^+ , Ar^{2+} , Ti^+ , Ti^{2+} , O^+ and O^{2+} in the DCMS (a), (e), HiPIMS (b), (f) and BPH (c) and (d), (g) and (h) discharges. For better visibility, the energy scale of the DCMS (a), (e) and HiPIMS (b), (f) conditions has been adapted in (i), (k) and (j), (l), respectively.

where ε is the ion energy, $F(\varepsilon)$ is the measured IEDF for either $\text{Ar}^{+/2+}$, $\text{O}^{+/2+}$ and $\text{Ti}^{+/2+}$.

In the DCMS and HiPIMS cases, the Ar^+ and Ti^+ time-averaged IEDFs exhibited energy tail extending up to ≈ 20 eV (DCMS) and ≈ 30 eV (HiPIMS) [39] (figures 4(a) and (b) or (i) and (j)) while, as expected, these values were higher for double charged ions, i.e. ≈ 32 eV for Ar^{2+} ions (DCMS) and ≈ 40 eV for Ar^{2+} and Ti^{2+} ions (HiPIMS) (figures 4(e) and (f) or (k) and (l)). However, the energy tail of the O^+ IEDFs exhibited much higher values, up to ≈ 30 and ≈ 70 eV in DCMS and HiPIMS regimes, respectively.

The time-averaged IEDFs in reactive unipolar HiPIMS regime are widely reported in the literature [23, 39–41], such IEDFs present a high-energy tail generally extending up to several tens of eV. On the other hand, in the BPH case, a significant amount of single and double charged ions were detected and the IEDFs exhibit very high energy population (up to 900 eV) as shown in figures 4(g) and (h). Such observation was also recently reported by Keraudy *et al* [28]. More particularly, the IEDF of Ar^{2+} ions displayed consistent features as compared to Ar^+ (figures 4(c) and (d)), i.e. a low-energy peak 0–40 eV followed by a pronounced high-energy component which peaks at ≈ 600 eV for Ar^{2+} ions. This behavior was similar for Ti^{2+} ions. It has also to be mentioned that the Ti^{2+} and O^{2+} signal intensities were found to be significantly lower than the Ar^{2+} one.

In addition, the Ti^+/Ar^+ ratio was equal to $\approx 0.2\%$ in the DCMS case (see table 2). In the HIP26A discharge, the ratio

Ti^+/Ar^+ was much higher ($\approx 26\%$) which is a typical feature of this regime [20] while it drastically decreased for the BPH26A discharge ($\approx 0.4\%$). Hence highlighting the predominance of gaseous ions detected at the mass spectrometer location in the BPH case (see black curves in figures 4(c) and (d)) as compared to the metal ion (red curves) resulting in a significant part of the energy supplied to the growing film by (fast) argon ions. Note that the $\text{Ti}^+/[\text{Ar}^+ + \text{O}^+]$ ratio exhibited the same behavior as shown in table 2. To get further insight into the variation of the ion fluxes in the BPH case as compared to the unipolar HiPIMS case, the ratio R of the total ion count (calculated by integrating the IEDF over the entire energy range), $R_{\text{BPH/HiP}}$, has been calculated using equation (4):

$$R_{\text{BPH/HiP}} = \frac{\int_0^\infty \varepsilon F_{\text{BPH}}(\varepsilon) d\varepsilon}{\int_0^\infty \varepsilon F_{\text{HiP}}(\varepsilon) d\varepsilon} \quad (4)$$

where ε is the ion energy and $F(\varepsilon)$ is the measured IEDF.

From equation (4), in the BPH26A discharge, we found $R_{\text{Ar}^+} = 470$ for Ar^+ ions, $R_{\text{O}^+} = 7$ for O^+ ions and $R_{\text{Ti}^+} = 3$ for Ti^+ ions. Hence, as the fraction is greater than one, it can be understood that applying the positive voltage, U_+ , increases the metal and gaseous ion flux reaching the mass spectrometer orifice in the BPH discharge as compared to the HiPIMS case. Moreover, it could be speculated that the high value of $R_{\text{BPH/HiP}}$ for Ar^+ ions could be attributed to an enhancement of the ionization degree of the argon gas, i.e. available in very large quantities in the plasma volume, due to electrons which are returning back to the cathode at the moment of positive voltage ignition as well as the presence of high kinetic energy ions of any nature (see figure 4).

Additionally, increasing the discharge peak current in the BPH case decreases the average energy $\langle \varepsilon \rangle$ of the metal ions ($\approx 10\%$) highlighting energy losses during the transport in the plasma phase. As discussed in our previous paper [30] in the metallic regime, these energy losses could be attributed to the angular distribution of the sputtered species in highly energetic regime [42] affecting the transport and detection of the charged species by the grounded head of the mass spectrometer.

The averaged kinetic energies, $\langle \varepsilon \rangle$, calculated using equation (3) for the various plasma ions probed in this study are reported in table 2 showing that $\langle \varepsilon \rangle$ for gas and metal ions are consistent with the literature when comparing DCMS and HiPIMS discharges [39]: $\langle \varepsilon_{\text{Ti}^+} \rangle$ slightly increased from 6.4 to 7.2 eV. In the BPH case, U_+ dramatically increases the average energy of single and double charged ions ranging from 132 to 280 eV and 54 to 583 eV, respectively, as shown in table 2. On the other hand, the maximum energy of gaseous ions in BPH discharges (higher than the corresponding U_+) can be partially explained by the overvoltage, approximately 500 V as shown in figure 2, appearing during a short time at the moment when U_+ is applied at the target resulting in an energy shift toward higher values.

In addition, the contribution of the high energy population to the total ion account is presented in table 3 hence highlighting a substantial fraction of gas ions (mainly argon) accelerated with U_+ correlating well with the observations of

Table 3. High energy ion population (200–400 eV) on the total ion flux (0–600 eV) ratio calculated for both BPH condition with $U_+ = 300$ V.

	$\frac{Ar_{200-400\text{ eV}}^+}{Ar^+}$ (%)	$\frac{Ti_{200-400\text{ eV}}^+}{Ti^+}$ (%)	$\frac{O_{200-400\text{ eV}}^+}{O^+}$ (%)
BPH26A	66	65	43
BPH70A	93	59	53

Viloan *et al* [32] who studied the reactive sputter deposition of TiN. Concomitantly, sputtered material can be accelerated and transported radially away from the cathode and lost to the walls [43] resulting in the slight decrease (from 65% to 59%) of the high energy Ti population on the total Ti flux ratio as shown in table 3. Likewise, due to the increase of the average ion energy in the BPH case, the radial acceleration of a higher amount of charged species during τ_+ could affect the deposition rate as discussed in the next section.

3.2. Deposition rate

The absolute static deposition rates R_D , defined as the thickness of deposited film per time unit [44] are summarized in table 2.

In the DCMS case, $R_D = 0.78$ nm·min⁻¹ whereas, with HiPIMS, R_D was lowered at the same average power to 0.55 and 0.21 nm·min⁻¹ in the HIP26A and HIP70A discharges, respectively. Such decrease being consistent with the unipolar HiPIMS literature [44–46]. In the BPH case, however, R_D is further reduced by $\approx 10\%$ as compared to the HiPIMS case. Similar behavior was observed if R_D is divided by the power applied to the discharge which was not exactly 100 W for BPH plasma (not shown here). In addition, it is shown that the deposition rates extracted from RBS measurements (expressed in atcm⁻²·s⁻¹) feature the same trend to those calculated from mechanical profilometer data (see table 2).

It is known that the deposition rates achieved in HiPIMS discharges are typically a fraction of those achieved during DCMS [20]. In the case of reactive sputtering of TiO₂ from a Ti target, a large disparity in the HiPIMS-to-DCMS deposition rate ratio can be found in the literature [47, 48], typically from 0.3 to 1.2. Regarding the BPH discharges, few deposition rate values [31, 33] were reported. For instance, R_D appeared to decrease ($\approx 15\%$) by increasing the positive reverse voltage U_+ (from 0 to 200 V) as observed by Velicu *et al* [31] during BPH operation mode. Considering the densification effect of the deposited thin films due to high energetic bombardment, the total deposition flux at the substrate was estimated to remain constant whatever the value of the positive target voltage. These authors concluded that the gravimetric deposition rates remained nearly unaffected by the increase of the positive target voltage. On the other hand, the deposition rates of Cu films across the center-line length of a rectangular Cu target were studied by Wu *et al* [33]. They showed that the increase of U_+ and τ_+ can improve R_D ($\approx 10\%$) as compared to the unipolar HiPIMS regime but with values still lower than for the corresponding DCMS case. Finally, a small

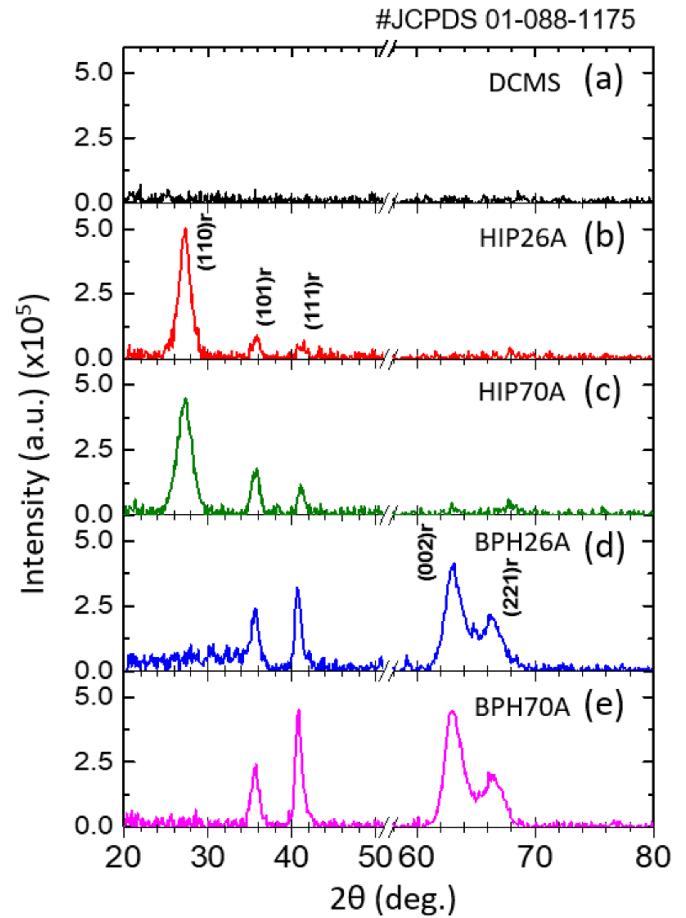


Figure 5. Grazing incidence x-ray diffraction patterns of ≈ 100 nm thick TiO₂ films grown on silicon substrates for various sputtering plasmas: (a) DCMS, (b) HIP26A, (c) HIP70A, (d) BPH26A and (e) BPH70A. The break in the x -axis is made to avoid displaying the intense diffraction line coming from the silicon single crystal used as substrate.

($\approx 15\%$) decrease of R_D was indicated by Viloan *et al* [32] as U_+ increases from 0 to 150 V. The main part of this decrease occurred already when applying +10 V. Large disparities of R_D in the BPH case are found from these various reports, involving different materials and deposition conditions. On the other hand, it is generally admitted that bombarding growing films by high energy ions (i.e. with kinetic energies higher than 200 eV) is usually not recommended for thin film deposition, since film re-sputtering and subsequent drop of R_D become probable.

3.3. Film properties

As discussed in section 3.1, the contribution of the high energy species could result in modification of the microstructure, texture and surface morphology as reported in several publications [15, 49, 50]. In this regard, the GIXRD patterns of ≈ 100 nm thick TiO₂ films grown at 5 mTorr on silicon wafers are shown in figure 5.

The TiO₂ film grown in DCMS regime was amorphous (figure 5(a)) while the GIXRD patterns corresponding to the

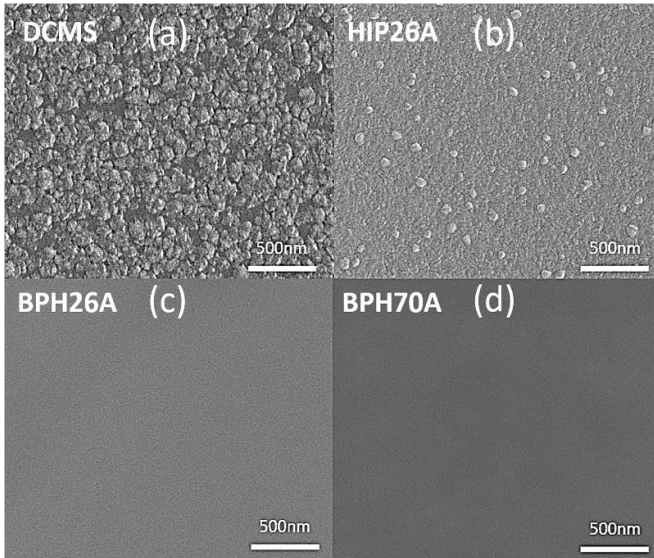


Figure 6. SEM micrographs showing surface roughness of TiO₂ films deposited on silicon substrates in DCMS (a), HiPIMS (b) and BPH (c) and (d) regimes.

samples grown with HiPIMS (see figures 5(b) and (c)) exhibited an intense (110) rutile peak at the angle of 27.9°. Weaker rutile peaks could also be observed in the angular range 35°–42°. For both BPH samples (see figures 5(d) and (e)), however, high intensity peaks appeared at 63.2° and 66.2° which could be attributed to the rutile (002) and (221) peaks, respectively, while the (110) peak is absent suggesting that the nucleation and growth of TiO₂ films were affected by the deposition conditions [14]. The enhancement of high angle peaks could be related to (argon) doping effects which could greatly influence the growth orientation as similarly observed by Xu *et al* [51] in the case of N-doped TiO₂ coatings. Nevertheless, further investigations are required to obtain a deeper understanding of the film growth in BPH regime.

On the other hand, the sputtering regime also affects the TiO₂ film topography as shown in figure 6. Operating at low ion energies, as in the DCMS case, leads to rather porous films (figure 6(a)) whereas energetic ion bombardment during the film growth promotes denser films with smoother surfaces [50] (figures 6(b)–(d)). Indeed, in this case, impinging ions have enough energy to enhance adatom mobility, leading to the densification of the material as discussed by Anders [52].

In addition, the RMS roughness of our films was studied by AFM and the data are summarized in table 4 for 1 × 1 μm² scan windows. The highest value of RMS roughness (12.85 nm) was found for the DCMS sample which is typical for low energetic deposition conditions while lower and similar values (≈1.4 nm) were found for the HIP26A, HIP70A and BPH26A samples, considering the experimental error. Furthermore, in the BPH70A case, the RMS roughness was slightly decreased (0.78 nm) showing that intense and energetic ion bombardment may promote very low film surface roughness which can be related to re-sputtering of the

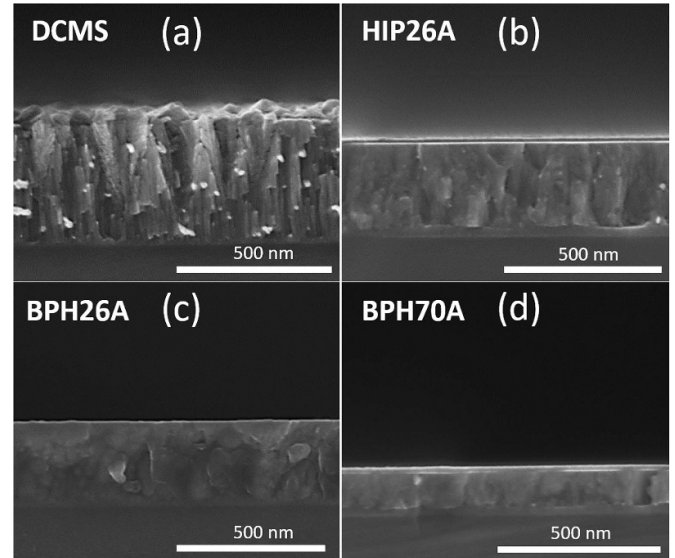


Figure 7. SEM micrographs showing fractured cross section of TiO₂ films synthesized in DCMS (a), HiPIMS (b) and BPH (c) and (d) regimes. Thicker TiO₂ films of ≈430 nm (a), ≈290 nm (b), ≈310 nm (c) and ≈140 nm (d) synthesized in the same plasma conditions are shown.

growing TiO₂ surface [53, 54] while, at the same time, the crystallite size increased from ≈3 to ≈10 nm (see table 4). Additionally, the cross sectional SEM micrographs of thicker TiO₂ films synthesized in the same conditions support the notion of microstructural densification of the films with energetic plasma conditions (figure 7). Such a microstructural change can be explained by the intensified ion-induced adatom mobility and suggests a transition from zone T (DCMS film) to zone 2 (HiPIMS films) to reach zone 3 in the case of BPH depositions, as referred to the structure zone diagram [44].

Besides, the film density as well as the density of defects in the material (e.g. the incorporation of argon in the film) may be modified if high energy Ar⁺ ions impinge on the film surface [55]. RBS data given in table 5 show that larger amounts of argon atoms were incorporated in the deposited layer in the BPH case (≈2.5%) as compared to HiPIMS (≈0.1%–0.4%) and DCMS (≈0.01%) regimes. These results are in line with the presence of highly energetic argon ions in the plasma phase [31] highlighted by our mass spectrometry measurements (see section 3.1).

From these RBS data, the film density, D , was determined using equation (5) by summing the Ti, O and Ar elemental densities (other detected elements were not considered because of the low content in the film) as:

$$D = \sum_{el.} \frac{T_{RBS} M}{N_A T_F} \quad (5)$$

where T_{RBS} is the equivalent thickness (expressed in thin film units, i.e. 10¹⁵ at cm⁻²), M is the atomic mass (expressed in amu), N_A is the Avogadro number, T_F is the film thickness measured by Dektak profilometer.

Table 4. AFM RMS roughness, average crystallite size, refractive index at 550 nm measured by spectroscopic ellipsometry and porosity calculated from ellipsometry data of amorphous and rutile TiO₂ films deposited by DCMS, HiPIMS or BPH. AFM images are available in the supplementary materials.

	Phase	Thick (nm)	Rough (nm)	Cryst. size (nm)	n_{550}	Ellip. por. (%)
DCMS	Amorp.	106 ± 2	12.85 ± 0.07	—	2.41	—
HIP26A	Rutile	111 ± 4	1.37 ± 0.25	3.6	2.53	29
HIP70A	Rutile	98 ± 3	1.48 ± 0.12	2.7	2.73	17
BPH26A	Rutile	109 ± 2	1.27 ± 0.34	10.7	2.49	31
BPH70A	Rutile	121 ± 11	0.78 ± 0.38	9.9	2.60	23

Table 5. Chemical composition of TiO₂ films deposited on silicon wafers measured by RBS analysis. Thin film unit (TFU) corresponds to 10¹⁵ atoms cm⁻². The film density, D , was determined from RBS measurements by summing the Ti, O and Ar elemental densities.

	Ti (TFU)	O (TFU)	Ar (TFU)	$\frac{\text{Ti}}{\text{O}}$ (%)	$\frac{\text{Ar}}{\text{Ti} + \text{O}}$ (%)	Density (g·cm ⁻³)
DCMS	272	604	0	45 ± 3	0.0 ± 0.0	3.6 ± 0.1
HIP26A	325	659	4	49 ± 2	0.4 ± 0.0	3.9 ± 0.1
HIP70A	282	621	1	45 ± 2	0.1 ± 0.0	4.0 ± 0.1
BPH26A	273	561	23	49 ± 2	2.7 ± 0.3	3.5 ± 0.1
BPH70A	324	626	24	52 ± 3	2.6 ± 0.2	3.6 ± 0.3

It was found that, as reported in table 5, $D = 3.6 \text{ g cm}^{-3}$ for the amorphous DCMS sample which is typical of low energetic conditions. This DCMS density value was lower than the ones of the rutile HiPIMS samples ($D = 3.9 \text{ g cm}^{-3}$ and $D = 4.0 \text{ g cm}^{-3}$ for HIP26A and HIP70A, respectively), closely matching the reported density of bulk rutile TiO₂ [56] (4.17 g cm^{-3}). In the BPH case, the film density was lowered as compared to the HiPIMS samples for both BPH conditions (3.5 and 3.6 g cm^{-3} for the BPH26A and BPH70A samples, respectively).

In addition, the Ti/O ratio was also calculated from RBS measurements (see table 5). The latter was not significantly affected by U_+ in the case of the BPH26A discharge (Ti/O = 0.49 in both HiPIMS and BPH cases) while this ratio seems to increase in the BPH70A discharge (considering the error bar), as compared to the HiP70A case, from 0.45 to 0.52 which could be explained by the re-sputtering of the deposited material during the deposition process [57] and in particular the preferential sputtering of O atoms as calculated in figure 8. The latter displays the sputter yields of a thin (100 nm) TiO₂ layer bombarded by energetic Ar and Ti ions as calculated by the Monte-Carlo-based TRansport of Ions in Matter [58] (TRIM) code. The $\approx 7 \text{ eV}$ ions produced in DCMS and HiPIMS plasmas (figure 4) do not cause any sputtering of the film whereas, in the BPH regime, re-sputtering by both Ar and Ti incident ions become probable as the average ion energy is dramatically increased in this case. Consequently, due to the preferential sputtering of oxygen, the TiO_x film grown under BPH70A conditions appears to be under-stoichiometric (TiO_{1.9}) in comparison to the other conditions (TiO_{2.0–2.2}). Concomitantly, the re-sputtering of the growing film in the BPH70A discharge leads to reduced film deposition rate, as previously discussed and presented in table 2.

This study highlights the effect of an intense ion bombardment during film growth on the crystalline constitution, film morphology and density which ultimately may modify the

optical characteristics of the TiO₂ coatings, the latter being analyzed by ellipsometry in the next section.

3.4. Optical properties

The refractive indices of the TiO₂ films at $\lambda = 550 \text{ nm}$, denoted as n_{550} , were evaluated from spectroscopic ellipsometry measurements and summarized in table 4. The optical thicknesses of the TiO₂ layers corresponded to those measured by Dektak mechanical profilometer. The thickness of the SiO₂ underlying the TiO₂ coating varied from 13 to 18.2 nm. We found that, at $\lambda = 550 \text{ nm}$, the refractive index corresponding to the DCMS coating ($n = 2.41$) was below those measured for the HIP26A ($n = 2.53$) and HiP70A ($n = 2.73$) deposited films, such behavior being consistent with the literature [7, 9, 59, 60]. However, the refractive index was slightly decreased for both BPH samples as compared to the HiPIMS samples, i.e. $n = 2.49$ for the BPH26A sample and $n = 2.60$ for the BPH70A sample.

It is known that the refractive index can be influenced by the film thickness as well as the density of pores within the films [6]. On the other hand, trapping of the sputtering gases in growing films [61] (as observed in section 3.3) can also result in the decrease of the refractive index as observed by Wei *et al* [62]. It has to be mentioned that the refractive index at $\lambda = 550 \text{ nm}$ of TiO₂ thin films is generally found between $n = 1.7$ and $n = 2.7$ [2, 60] while $n = 2.849$ was reported by Tanemura *et al* [63] for RF-MS deposited rutile TiO₂ films, such value being explained by the fine crystallinity of the samples. Accordingly, the porosity P of our films was calculated using the following equation [64]:

$$P = \left(1 - \frac{n_c^2 - 1}{n_d^2 - 1} \right) \times 100(\%) \quad (6)$$

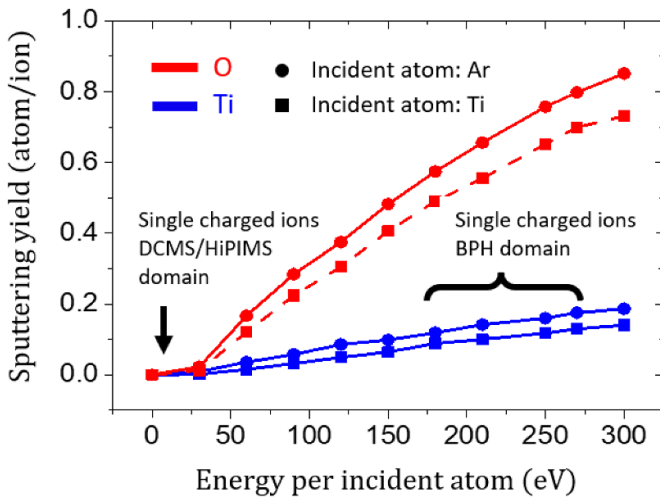


Figure 8. Sputter Yields calculations of a 100 nm thick TiO_2 layer using TRIM software. The presented values are calculated for Ar (solid circles) and Ti (solid squares) incident atoms as a function of their average energy.

where n_d is the value obtained for a rutile TiO_2 single crystal [65] ($n_d = 2.95$ at $\lambda = 550$ nm) and n_c is the measured refractive index of the TiO_2 film.

Unipolar HiPIMS regime promotes lower film porosity ($P \approx 17\%$) as reported in table 4. In the BPH case, however, the porosity increased to $P \approx 31\%$ with BPH26A and $P \approx 23\%$ with BPH70A. This behavior was found to be in good agreement with the film density values calculated from RBS measurements as reported in table 5. Moreover, as shown in figure 9, a qualitative correlation is established in the variation of the refractive index measured by spectroscopic ellipsometry (blue curve) and the density of the TiO_2 films (red curve) calculated from RBS measurements.

The increase in porosity observed under high energetic deposition conditions could be attributed to the formation of defects, e.g. vacancies resulting in the shift in stoichiometry and maybe others [66], as discussed in section 3.3 (the Ti/O ratio in the film being equal to 52% for the BPH70A condition), this hypothesis nevertheless requires further investigations. In our conditions, the amorphous, columnar and porous DCMS film is characterized by the lowest refractive index while the low porosity of the HiPIMS coatings results in the highest refractive index ($n = 2.73$ at $\lambda = 550$ nm). Furthermore, the BPH films are characterized by lower refractive indices as compared to the HiPIMS ones which is mainly attributed to the incorporation of argon within the films and other defects. In the next section, the properties of virtual films modeled by kinetic Monte Carlo calculations, through the NAnoSCALE Modeling (NASCAM) code, were compared to the experimentally grown films.

3.5. NASCAM modeling

The mass spectrometry results summarized in table 6 served as input data for kinetic Monte Carlo-based simulations performed with the NAnoSCALE Modeling (NASCAM) code.

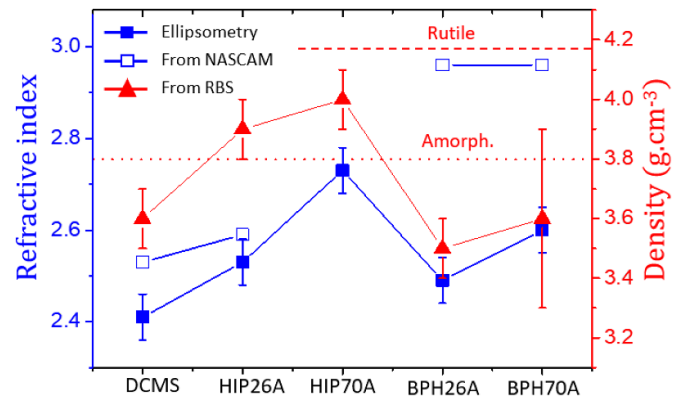


Figure 9. Refractive indices, n (solid blue squares), of 100 nm thick TiO_2 coatings measured at $\lambda = 550$ nm by spectroscopic ellipsometry and calculated ones, n_{model} (empty blue squares), using NASCAM software package (based on the Bruggeman effective medium theory). The density of TiO_2 films (solid red triangles), extracted from RBS measurements, is shown as well as the reported (calculated) density values of bulk rutile TiO_2 [65] and amorphous TiO_2 [68].

Knowing the ion fluxes reaching the substrate (see section 3.1), it was nevertheless necessary to estimate the flux of Ti and O neutrals to the substrate. In this regard, based on kinetic theory of gases, the oxygen flux was calculated assuming fully thermalized particles. The energy and velocity distribution of Ti neutrals was also calculated at the substrate position considering collisions of Ti atoms with the plasma gas on their path from the target to the substrate. Such distributions were calculated thanks to the SIMTRA code [67] (data not shown) considering the deposition geometry used in this study. If the ionization rate is known for one of the species, then one can link the flux of neutrals to the fluxes of ions. It was assumed that the ionization rate of Ti was equal to 0.1 for DCMS discharge and about 0.8 for HiPIMS discharge as measured by Konstantinidis *et al* in previous works [69] resulting in the relative amount of Ti atoms and Ti ions shown in table 6.

The substrate size was 100×10 atomic cells and the total number of deposited atoms were about 1.0×10^6 in order to obtain ≈ 100 nm thick films. In the BPH case, NASCAM simulation highlighted the role of Ar flux causing sputtering and densification of the film (see table 6) resulting in a total number of deposited atoms up to 1.2×10^6 for the HiPIMS/BPH discharges.

The optical properties of the coatings were calculated based on the Bruggeman effective medium theory allowing the computation of the refractive index at $\lambda = 550$ nm of the TiO_2 coatings, n_{model} , as shown in figure 9. The n_{model} values were compared to the refractive indices measured by spectroscopic ellipsometry. Note that, as the NASCAM code can only simulate amorphous coatings, one cannot expect significant difference in the optical properties of the TiO_2 films simulated in both HiPIMS and BPH cases. Nevertheless, we found at $\lambda = 550$ nm, $n_{model} = 2.53$ and $n = 2.41$ for the DCMS case, this later value being slightly higher than the literature values (≈ 2.2 – 2.3 [9, 70]). In the HIP26A case, $n_{model} = 2.59$ and $n = 2.53$, such values being close and consistent with

Table 6. Relative amount of atoms and ions coming to the substrate for different deposition conditions (calculated from the metal-to-gas ratios shown in table 2). The relative TiO₂ film densities calculated using NASCAM package are also shown.

	Ti	Ti ⁺	O ⁺	Ar ⁺	Rel. dens. value
DCMS	1	0.11	23.1	46.3	0.8
HIP26A	1	4	53.6	15.4	0.97
BPH26A	1	4	238	1052	1.0
BPH70A	1	4	94.8	53.3	1.0

the literature [9]. In the BPH case, n_{model} value was found to be the highest ($n_{model} = 2.96$) while, contrariwise, it is the HiPIMS film that exhibits the highest measured refractive index.

The significant increase of n_{model} in the BPH case can be correlated to the increase of the calculated density of the BPH films (see table 6). In contrast, the measured densities of the HiPIMS samples are clearly higher than those of the BPH samples (see red solid triangles in figure 9) resulting in the decrease of n for the BPH samples (see blue solid squares in figure 9). This highlights that the film density is a key parameter regarding the variation of the measured and simulated refractive indices in the present study. On the other hand, because NASCAM cannot simulate argon trapping properly, this might also explain the high n_{model} calculated for the BPH discharges as compared to the measured refractive indices, n , correlating well with the study of Wei *et al* [62] who observed a decrease in the refractive index for several lithium niobate samples due to argon implantation.

Consequently, the experimentally measured refractive indices are in good agreement with the simulated ones, excepted for the BPH case which is mainly explained by the significant amount of trapped argon atoms inside the film for this particular condition.

4. Conclusion

TiO₂ films were deposited in a broad range of discharge conditions including DCMS, HiPIMS and BPH processes and a detailed plasma and thin film characterization was carried out. From the data presented in this work, several conclusions can be drawn.

It is found that the crystalline constitution of the TiO₂ films is intimately correlated to the plasma discharge characteristics and energy supplied to the growing film. Our data show that the phase constitution evolves from amorphous, for the coatings synthesized by DCMS, to pure rutile films in the case of HiPIMS discharge. Ultimately, the x-ray diffraction pattern of the rutile films is characterized by the presence of peaks at higher angles for the highly energetic BPH case. Beside crystalline constitution, film morphology, density, and surface roughness also vary. Furthermore, in the case of the BPH process with +300 V positive voltage applied after the negative pulse, argon trapping in the layer becomes significant, and a slight increase of the Ti/O ratio is observed. Cross sectional SEM observation of the films deposited in this condition appears to demonstrate the formation of dense

structures with low surface roughness. Nevertheless, ellipsometric investigations show that low porosity films synthesized under HiPIMS condition exhibit the highest refractive index ($n = 2.73$ at $\lambda = 550$ nm) while it is found to be lower with the BPH process.

Finally, NASCAM modeling predicts that the films virtually deposited under BPH conditions should have the highest density because of the intense ion bombardment. Ultimately, re-sputtering of the film occurred therefore promoting a lower deposition rate. This behavior was in good agreement with experimental observations. We have also shown that refractive indices were strongly dependent on the synthesis method and energy supplied to the growing film.

This study further contributes to a comprehensive understanding of the correlation between the process parameters, the plasma phase, and the film properties. Our results highlight the importance of tailoring the discharge electrical parameters. Finally, it should also be mentioned that a well-studied magnetic geometry combined with finely tuned electrical parameters can improve the deposition rate and other films properties. This topic is of a particular interest for bipolar magnetron sputtering and will be studied in the near future.

Data availability statement

The data that support the findings of this study are available upon reasonable request from the authors.

Acknowledgments

S Konstantinidis is senior research associate of the 'Fonds de la Recherche Scientifique' (F.R.S.-FNRS, Belgium). The authors would like to thank the Walloon Region of Belgium and the European Regional Development Fund for financial support through the Diag&Growth project. Discussions with Prof Dr D Depla (Ghent University), R Dedoncker (Ghent University), Dr D Moerman (Materia Nova) and L Yonge (Materia Nova) were also strongly appreciated.

ORCID iDs

M Michiels  <https://orcid.org/0000-0003-3028-1520>
 T Godfroid  <https://orcid.org/0000-0003-4124-6392>
 S Lucas  <https://orcid.org/0000-0003-3229-9855>
 R Snyders  <https://orcid.org/0000-0001-8164-346X>
 S Konstantinidis  <https://orcid.org/0000-0002-1672-309X>

References

- [1] Adawiyah J H, Zainab N J and Imad H A 2019 *Energy Proc.* **157** 17–29
- [2] Martinu L and Poitras D 2000 *J. Vac. Sci. Technol. A* **18** 2619–45
- [3] Panepinto A, Michiels M, Duerrschabel M, Molina-Luna L, Bittencourt C, Cormier P A and Snyders R 2019 *ACS Appl. Energy Mater.* **3** 759–67
- [4] Hanaor D and Sorrell C 2011 *J. Mater. Sci.* **46** 855–74
- [5] Loebel P, Huppertz M and Mergel D 1994 *Thin Solid Films* **251** 72–9
- [6] Evtushenko Y, Romashkin S, Trofimov N and Chekhlova T 2015 *Phys. Proc.* **73** 100–7
- [7] Prabitha B N, Justinivictor V, Daniel G, Joy K, Raju J, Kumar D and Varkey P 2014 *Prog. Nat. Sci.: Mater. Int.* **24** 218–25
- [8] Periyat P, Naufal B and Ullattil S 2016 *Mater. Sci. Forum* **855** 78
- [9] Konstantinidis S, Dauchot J and Hecq M 2006 *Thin Solid Films* **515** 1182–6
- [10] Davidsdottir S, Shabadi R, Galca A, Andersen I H, Dirscherl K and Ambat R 2014 *Appl. Surf. Sci.* **313** 677–86
- [11] Toyoda T and Yabe M 2000 *J. Phys. D: Appl. Phys.* **16** L251
- [12] Sangchay W, Lek S and Kooptarnond K 2012 *Proc. Eng.* **32** 590–6
- [13] Su R, Bechstein R, SØ L, Vang R, Sillassen M, Esbjörnsson B, Palmqvist A and Besenbacher F 2011 *J. Phys. Chemis. C* **115** 24287–92
- [14] Asanuma T, Matsutani T, Liu C, Mihara T and Kiuchi M 2004 *J. Appl. Phys.* **95** 6011–16
- [15] Cemin F, Tsukamoto M, Keraudy J, Antunes V, Helmersson U, Alvarez F, Minea T and Lundin D 2018 *J. Phys. D: Appl. Phys.* **51** 235301
- [16] Cormier P A, Balhamri A, Thomann A L, Dussart R, Semmar N, Lecas T, Snyders R and Konstantinidis S 2014 *Surf. Coat. Technol.* **254** 291–7
- [17] Nouvellon C et al 2012 *Surf. Coat. Technol.* **206** 3542–9
- [18] Bobzin K, Brögelmann T, Kruppe N and Engels M 2016 *Thin Solid Films* **620** 188–96
- [19] Ferrec A, Keraudy J, Jacq S, Schuster F, Jouan P Y and Djouadi M 2014 *Surf. Coat. Technol.* **250** 52–6 4th Int. Conf. on Fundamentals and Applications of HIPIMS and Final Event of COST Action MP0804 Highly Ionized Pulse Plasma Processes—HIPPP Processes
- [20] Sarakinos K, Alami J and Konstantinidis S 2010 *Surf. Coat. Technol.* **204** 1661–84
- [21] Samuelsson M, Lundin D, Jensen J, Raadu M A, Gudmundsson J T and Helmersson U 2010 *Surf. Coat. Technol.* **205** 591–6
- [22] Samuelsson M, Lundin D, Sarakinos K, Björefors F, Wälivaara B, Ljungcrantz H and Helmersson U 2012 *J. Vac. Sci. Technol. A* **30** 031507–1
- [23] Anders A 2017 *J. Appl. Phys.* **121** 171101
- [24] Thomann A L, Caillard A, Raza M, Mokh M, Cormier P A and Konstantinidis S 2019 *Surf. Coat. Technol.* **377** 124887
- [25] Graillot-Vuillecot R, Thomann A L, Lecas T, Cachoncinlle C, Millon E and Caillard A 2020 *Vacuum* **181** 109734
- [26] Britun N, Michiels M and Godfroid T 2018 *Appl. Phys. Lett.* **112** 234103
- [27] Hippler R, Čada M and Hubička Z 2020 *Appl. Phys. Lett.* **116** 064101
- [28] Keraudy J, Viloan R P B, Raadu M A, Brenning N, Lundin D and Helmersson U 2019 *Surf. Coat. Technol.* **359** 433–7
- [29] Kozák T, Pajdarová A, Čada M, Hubička Z, Mareš P and Capek J 2020 *Plasma Sources Sci. Technol.* **29** 065003
- [30] Michiels M, Godfroid T, Snyders R and Britun N 2020 *J. Phys. D: Appl. Phys.* **53** 435205
- [31] Velicu I L, Ianoş G T, Porosnicu C, Mihaila I, Burducea I, Alin V, Cristea D, Munteanu D and Tiron V 2018 *Surf. Coat. Technol.* **359** 97–107
- [32] Viloan R P, Gu J, Boyd R, Keraudy J, Li L and Helmersson U 2019 *Thin Solid Films* **688** 137350
- [33] Wu B, Haehnlein I, Shchelkanov I, McLain J, Patel D, Uhlig J, Jurczyk B, Leng Y and Ruzic D N 2018 *Vacuum* **150** 216–21
- [34] Greczynski G and Hultman L 2010 *Vacuum* **84** 1159–70
- [35] Hamers E, van Sark W, Bezemer J, Goedheer W and Weg W 1998 *Int. J. Mass Spectrom. Ion Processes.* **173** 91–8
- [36] Barradas N P, Jaynes C and Webb R P 1997 *Appl. Phys. Lett.* **71** 291–3
- [37] Gurbich A 2016 *Nucl. Instrum. Methods Phys. Res. B* **371** 27–32
- [38] Tonneau R, Moskovkin P, Pflug A and Lucas S 2018 *J. Phys. D: Appl. Phys.* **51** 195202
- [39] Aiempantak M, Helmersson U, Aijaz A, Larsson P, Magnusson R, Jensen J and Kubart T 2011 *Surf. Coat. Technol.* **205** 4828–31
- [40] Jouan P Y, Brizoual L, Ganciu M, Cardinaud C, Tricot S and Djouadi A 2010 *IEEE Trans. Plasma Sci.* **38** 3089–94
- [41] Tiron V, Velicu I L, Cristea D, Lupu N, Stoian G and Munteanu D 2017 *Surf. Coat. Technol.* **352** 690–8
- [42] Capek J, Hala M, Zabeida O, Klemberg-Sapieha J and Martinu L 2012 *J. Phys. D: Appl. Phys.* **45** 205205
- [43] Lundin D, Larsson P, Wallin E, Lattemann M, Brenning N and Helmersson U 2008 *Plasma Sources Sci. Technol.* **17** 035021
- [44] Anders A 2010 *J. Vac. Sci. Technol. A* **28** 783
- [45] Brenning N, Huo C, Lundin D, Raadu M, Vitelar C, Stancu G, Minea T and Helmersson U 2012 *Plasma Sources Sci. Technol.* **21** 025005
- [46] Helmersson U, Lattemann M, Bohlmark J, Ehiastian A and Gudmundsson J 2006 *Thin Solid Films* **513** 1–24
- [47] Alami J, Maric Z, Busch H, Klein F, Grabow U and Kopnarski M 2014 *Surf. Coat. Technol.* **255** 43–51
- [48] Davis W, Christie D and Geisler M 2004 *47th Annual Technical Conf. of Society of Vacuum Coaters 24–29 April 2004 Dallas, TX* vol 215 pp 215–8
- [49] Ji H, Was G S, Jones J W and Moody N R 1997 *J. Appl. Phys.* **81** 6754–61
- [50] Amin A, Kohl D and Wuttig M 2010 *J. Phys. D: Appl. Phys.* **43** 405303
- [51] Xu J, Xu L, Wang J T and Selloni A 2017 Titanium Dioxide M Janus (<https://doi.org/10.5772/intechopen.69141>)
- [52] Anders A 2010 *Thin Solid Films* **518** 4087–90
- [53] Vergöhl M, Werner O and Bruns S 2008 *Proc. SPIE - Int. Soc. Opt. Eng.* **7101**
- [54] Tiron V, Ursu E L, Cristea D, Munteanu D, Bulai G, Ceban A and Velicu I L 2019 *Appl. Surf. Sci.* **494** 871–9
- [55] Cevro M 1995 *Thin Solid Films* **258** 91–103
- [56] 2007 CRC Handbook 88th edn (Boca Raton, FL: CRC Press) p 4–96
- [57] Theirich D and Engemann J 1991 *Nucl. Instrum. Methods Phys. Res. B* **59–60** 336–40
- [58] Greene J P, Nemanich J, Thomas G E and Schiel S L 1997 *Nucl. Instrum. Methods Phys. Res. A* **397** 91–8
- [59] Richards B 2003 *Sol. Energy Mater. Sol. Cells* **79** 369–90
- [60] Simionescu O, Romanitan C, Tutunaru O, Ion V, Buiu O and Avram A 2019 *Coatings* **9** 442
- [61] Greene J E, Barnett S A, Sundgren J E and Rockett A 1989 Low-energy ion/surface interactions during film growth from the vapor phase *Ion Beam Assisted Film Growth T Itoh* (Amsterdam: Elsevier) pp 101–52

- [62] Wei D T Y, Lee W W and Bloom L R 1974 *Appl. Phys. Lett.* **25** 329–31
- [63] Tanemura S, Miao L, Jin P, Kaneko K, Terai A and Nabatova-Gabain N 2003 *Appl. Surf. Sci.* **212** 654–60
- [64] Paul W 1959 *J. Phys. Chem. Solids* **10** 345–6
- [65] DeVore J R 1951 *J. Opt. Soc. Am.* **41** 416–19
- [66] Silversmit G, Poelman H and De Gryse R 2004 *Surf. Interface Anal.* **36** 1163–6
- [67] Aeken K, Mahieu S and Depla D 2008 *J. Phys. D: Appl. Phys.* **41** 205307
- [68] Prasai B, Cai B, Rice M, Lewis J and Drabold D 2012 *J. Mater. Sci.* **47** 7515–21
- [69] Konstantinidis S, Dauchot J P, Ganciu M and Hecq M 2006 *Appl. Phys. Lett.* **88** 021501
- [70] Tomaszewski H, Poelman H, Depla D, Poelman D, Gryse R, Fiermans L, Reyniers M F, Heynderickx G and Marin G 2002 *Vacuum* **68** 31–8